Intra-cloud Microphysical Variability Obtained from Large-eddy Simulations using the Super-droplet Method

Toshiki Matsushima,[a] Seiya Nishizawa,[a] Shin-ichiro Shima,[a,b] and Wojciech W. Grabowski[c]

[a] *RIKEN Center for Computational Science, Kobe, Hyogo, Japan*
[b] *Graduate School of Simulation Studies, University of Hyogo, Kobe, Japan*
[c] *Center for Atmospheric Research, Boulder, Colorado*

ABSTRACT: In this study, the super droplet-method (SDM) is used in large-eddy simulations of an isolated cumulus congestus observed during the 1995 Small Cumulus Microphysics Study field project in order to investigate the intra-cloud variability associated with entrainment and mixing. The SDM is a Lagrangian particle-based method for cloud microphysics that provides droplet size distributions (DSD) coupled to the simulated cloud-scale dynamics. The authors show that sensitivity to the spatial resolution and the initial number of particles is larger, and sensitivity to the initial conditions is smaller, when the order of the DSD moment is smaller. Through the use of simulations with reliable statistics, microphysical variability is investigated at scales of ~ 100 m that can be considered well resolved in both the numerical simulations and in-situ aircraft observations. Large spatial variability in cloudy volumes is shown to be strongly affected by entrainment. Mean values of the adiabatic fraction (AF), cloud droplet number concentration, and the cubed ratio of the mean volume radius and the effective radius (k) agree well with observations in the middle and upper cloud layers. Moreover, the AF and k values are found to be positively correlated, and the reduction of the mean volume radius scaled by its adiabatic value with the decrease of the mean droplet concentration scaled by its adiabatic value is found to be smaller than the theoretical prediction of homogeneous mixing. The latter supports the notion of inhomogeneous mixing due to entrainment.

1. Introduction

In meteorology and climatology, one of the challenges related to clouds is understanding interactions over a wide range of spatial scales. Warm clouds are composed of a tremendous number of microscale water droplets. They can grow into large droplets in a short time by condensation and collisions depending on the surrounding environment (Siebert et al. 2006). At the same time, macroscopic cloud properties drive the large-scale circulation and affect the global radiation budget (Held et al. 2007). Accurate prediction of the droplet size distribution (DSD) can reduce uncertainty of weather and climate prediction (Stevens et al. 2005).

The effect of entrainment and mixing on the DSD depends on the ratio of the phase change time scale and the turbulent mixing time scale. When dry air flows into a cloud and rapidly mixes with the cloudy air, all droplets are exposed to the same subsaturation, and the DSD shifts to smaller sizes. The cloud droplet number concentration (CDNC) can decrease because small water droplets in the cloud evaporate preferentially. This regime is referred to as homogeneous mixing. On the other hand, if the evaporation time scale is smaller than the turbulence mixing time scale, the water droplets near the cloud–clear air interface evaporate completely without affecting the droplets away from the interface, which in turn reduces the CDNC. When such an air parcel is in an upward flow, the DSD shifts towards larger sizes due to the increase in the water vapor available for each droplet (Baker et al. 1980). In this regime, the mixing is referred to as inhomogeneous. Furthermore, when the cloud condensation nuclei (CCN) entrained into the cloud are newly activated, the DSD tends towards smaller sizes. The effects of turbulence also vary depending on the spatio-temporal evolution of cumulus-scale dynamics causing spatial variations of the DSD and its statistics (Arabas et al. 2009; Brenguier et al. 2011).

The flow inside clouds is turbulent. Such turbulence is considered to be a key factor for DSD prediction (Bodenschatz et al. 2010). Because of turbulent mixing and entrainment, temperature and water vapor fluctuate widely in clouds, in turn causing supersaturation fluctuations (e.g. Siebert and Shaw 2017). If droplets at a certain position inside a cloud display a large variety of growth histories because of these fluctuations, a broader DSD may result. This mechanism was initially proposed by Cooper (1989) and later called eddy-hopping by Grabowski and Wang (2013).

Lasher-Trapp et al. (2005) (hereinafter referred to as L05) showed for the first time that such a mechanism indeed contributes to the DSD width. They first simulated the cloud using a single-moment bulk cloud microphysics model. Then, using the simulated flow, they computed multiple backward trajectories reaching a selected location inside the cloud and assigned a Lagrangian parcel model to each of these trajectories. Each Lagrangian parcel model solved the condensational growth of droplets inside a parcel. The DSD at the location was computed as the ensem-

Corresponding author: Toshiki Matsushima, toshiki.matsushima@riken.jp

ble means of the droplet radius in the Lagrangian parcels. However, mixing between the parcels was not considered until they reached the same location and the mixing inside and outside the parcels was parameterized. Because the method did not provide a prognostic DSD across the entire cloud, it is difficult to compare the DSDs to those obtained by observation in a reliable way.

These problems can be resolved using the super-droplet method (SDM), a Lagrangian cloud microphysical scheme developed by Shima et al. (2009). In the SDM, a large ensemble of actual water droplets is represented as one super-droplet (SD). SDs are coupled to the dynamics and thermodynamics resolved by a large-eddy simulation, and the evolution of the properties of each SD is calculated along its trajectory. Using this method, it is possible to predict the DSD within a model grid box, including the influence of entrainment and turbulent mixing. Compared to a conventional bulk method, more complicated DSDs, such as multimodal distributions, can be represented using the SDM. In addition, the Lagrangian method eliminates the impact of numerical diffusion on the DSD shape as compared to the bin method (Morrison et al. 2018; Grabowski et al. 2019; Grabowski 2020a,b). The SDM also has the advantage of traceability that is similar to the Lagrangian parcel models (Heus et al. 2008; Yamaguchi and Randall 2012). The validity and physical performance of the SDM have been examined by idealized numerical simulations applying model setups from the Rain in Cumulus over the Ocean field campaign (RICO) (Arabas and Shima 2013), and from the Barbados Oceanographic and Meteorological Experiment (BOMEX) case (Sato et al. 2017, 2018). Their main focus was on comparing simulations among different model configurations, investigating grid convergence, and comparing with a double-moment bulk scheme.

The purpose of this study is to investigate the validity of the SDM by applying sensitivity simulations, comparing simulation results to observations, and considering cloud microphysical variability driven by entrainment and mixing. While microphysical variability at the grid scale has been investigated by Arabas and Shima (2013), we focus on spatial scales that correspond to well-resolved flow features. In this study, we exclude fluctuations due to unresolved subgrid-scale features considered in Grabowski and Abade (2017); Abade et al. (2018) and include only the impact of spatially resolved flow scales. Our numerical simulations are similar to Lasher-Trapp et al. (2001) (L01 hereinafter) and L05 using the SDM. The target case is the isolated cumulus congestus cloud observed on 22 July during the Small Cumulus Microphysics Study (SCMS) field campaign. The microphysical variability of the selected case was estimated from aircraft and X-band radar observations; we apply those data for model validation and comparison.

The remainder of the paper is organized as follows: Section 2reviews observations from the SCMS field campaign that will be used in subsequent comparisons with our simulation results. Section 3 describes the numerical model, presents the governing equations, and discusses design of numerical simulations. We also present a technique to analyze SD statistics by applying the kernel density estimation method. Results of our large-eddy simulations of the cumulus congestus cloud are discussed in section 4. Here, we examine the sensitivity of the simulated cloud dynamics and microphysics to the spatial resolution, the initial number of SDs, and the initial conditions. We also compare the simulated DSD statistics and their spatial variability to the observed values and show their relationship to microphysical parameters related to entrainment and mixing. Future prospects for grid convergence and entrainment/mixing studies are discussed in section 5. A summary is provided in section 6.

2. Small Cumulus Microphysics Study

In this section, we review the observational study of the SCMS field campaign based on Knight and Miller (1998); Hudson and Yum (2001); Brenguier et al. (2011) and L01, the results of which are used for comparison with the numerical simulations described in section 4. The SCMS field campaign took place from July to August 1995 near Cape Canaveral, Florida. Airborne and radar observations of cloud microphysical properties were collected targeting cumulus clouds. During this period, the direction of the lower tropospheric winds was slowly evolving, with westerly winds from the continent until July 25, followed by easterly winds from the ocean between July 26 and August 11, and back to westerly winds thereafter. CCN was sampled outside the clouds using the airborne instantaneous CCN spectrometer. The mean and standard deviation of the CCN number concentration at 1% supersaturation was $1411 \pm 388\,\mathrm{cm}^{-3}$ for the westerly winds, and $359 \pm 142\,\mathrm{cm}^{-3}$ for the easterly winds. The observed CDNC was also evolving over time in response to the CCN concentration changes. During the 11-day period, droplets with diameters between approximately 5 and 38 μm were sampled using an aircraft equipped with a Fast Forward Scattering Spectrometer Probe (Fast-FSSP) collecting data at 10 Hz (Brenguier et al. 1998). Since the speed of an aircraft is approximately $100\,\mathrm{m\,s}^{-1}$, a single sample can be regarded as representing statistics along an approximately 10 m flight path. The average CDNC varied in the range of 120–$329\,\mathrm{cm}^{-3}$.

Given the available information from the SCMS, we set the target day for our numerical simulations as 22 July, as in L01 and L05. On that day, the wind direction was about to change from westerly to easterly, and the averaged CCN at 1% supersaturation was approximately $1000 \pm 700\,\mathrm{cm}^{-3}$. Table 1 shows the statistics obtained from the aircraft observations. In addition to statistics for the target day, the maximum, minimum, and mean values during the entire

TABLE 1. Cloud microphysical characteristics during the SCMS field campaign (cited from Brenguier et al. 2011). The minimum, maximum, and mean values during the period are listed in the min, max, and mean rows, respectively.

	$\langle N \rangle \pm \sigma_N\,[\mathrm{cm}^{-3}]$	$\langle k \rangle \pm \sigma_k$	k^*	$\langle \mathrm{AF} \rangle$
22/07/1995	294 ± 243	0.825 ± 0.060	0.692	0.213
min	120	0.802	0.692	0.213
max	329	0.867	0.805	0.447
mean	217	0.831	0.753	0.306

SCMS field campaign are provided in order to confirm the relative degree of consistency between the observations and the numerical simulations described in section 4. In the table, N is the CDNC; $\langle N \rangle$ and σ_N are the mean and standard deviation of the local CDNC, respectively. The parameter k, the cubed ratio of the mean volume radius r_v and the effective radius r_e, that is, $k = r_v^3/r_e^3$, was originally introduced by Martin et al. (1994). $\langle k \rangle$ and σ_k represent the mean and standard deviation of their local values, respectively. Although k depends on the DSD shape (e.g., its skewness), typically the change in k is largely due to the change of the relative standard deviation. k^* is the cubed ratio of the mean volume radius and the mean effective radius for the entire cloud defined using horizontally and vertically averaged DSD moments. The adiabatic fraction (AF) is the ratio of the liquid water content (LWC) to the adiabatic LWC, and $\langle \mathrm{AF} \rangle$ is the average value of the local adiabatic fraction. The CDNC observed on 22 July was relatively high compared to other days because the air mass origin on that day was from the continent. Since the observed AF is the smallest on 22 July, the dilution by entrainment of environmental dry air is considered to be stronger than in the other cases. We note for our later comparisons with the observations that Brenguier et al. (2011) found k to have a positive trend against AF (Fig. 3 in their paper). They also found that the relationship holds between $\langle \mathrm{AF} \rangle$ and $\langle k \rangle$ (Fig. 4 in their paper). Such a relationship implies that the variability of k is strongly related to the entrainment and mixing.

Our target case for numerical simulations is the relatively isolated cumulus congestus observed around 1512 UTC (L01, L05). The cloud top evolved from 2 km to 5 km from 1512 UTC to 1540 UTC. The radar reflectivity factor observed by the X-band radar increased from −15 dBZ to 10 dBZ in 14 minutes from 1512 UTC. (Note that the uncertainty of the radar reflectivity factor is 2 dBZ to 3 dBZ.) The region with radar reflectivity larger than 0 dBZ was initially observed above 3.4 km height, and it later descended to 1.0 km height as a precipitation shaft. Figure 1 shows the skew-T log-P diagram of the sounding obtained close to where the cumulus congestus cloud was observed (cf. Fig. 1 in L01). At approximately 4.5 km height, there is a dry air mass with low dew point temperatures. The temperature is below 0 °C above the altitude of approximately

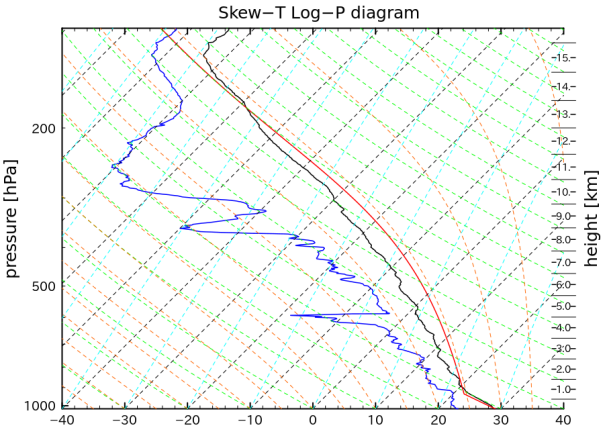

FIG. 1. Skew-T log-P diagram of the sounding taken on 22 July at 1545 UTC near Orlando. The constant temperature and dew point lines are indicated by the black and cyan dotted lines, respectively. The dry and moist adiabats are indicated by the green and orange lines, respectively. Temperature and dew point are shown by the black and blue lines, respectively. The red line shows temperature when the air parcel is adiabatically lifted.

5.05 km, close to the maximum cloud-top height. The level of neutral buoyancy is higher than the observed cloud-top height (approximately 13 km), suggesting that the effect of entrainment on the cloud dynamics is large.

3. Methods

a. Numerical Methods

SCALE-RM (Nishizawa et al. 2015; Sato et al. 2015) was used as the numerical model in this study. SCALE-RM adopts the fully compressible nonhydrostatic equations for the atmospheric flow in a Cartesian coordinate system (x, y, z), where x, y, z are the eastward, northward, and upward directions, respectively. The model's dynamical core applies a finite volume method using an Arakawa C-grid. SDM (Shima et al. 2009) was used as the cloud microphysical scheme. A Smagorinsky-Lilly type scheme including stratification effects (Brown et al. 1994) was used as the subgrid-scale (SGS) turbulence scheme.

In the SDM, each SD has a set of attributes to represent droplet characteristics that include droplet position, radius, mass of the solute aerosol, and multiplicity. The latter represents the number of real droplets in each SD. The processes describing time evolution of each SD include advection, activation/condensation, and collision-coalescence. The advection of each SD is computed assuming that the SD moves with the terminal velocity relative to wind velocity. The activation/condensation is represented by assuming that the SD radius R changes according to the Köhler

theory:

$$R\frac{dR}{dt} = \frac{1}{F_k + F_d}\left[S - \frac{a(T)}{R} + \frac{b(M)}{R^3}\right], \quad (1)$$

where M is the dry aerosols mass, T is the temperature, S is the supersaturation, t is time, and F_k and F_d depend on the heat conductivity and the vapor diffusivity, respectively. The term a/R represents the curvature effect, with a being a function of temperature. The term b/R^3 represents the solute effect, where b depends on the dissolved aerosol mass M. When a droplet is in equilibrium ($dR/dt = 0$), the equilibrium relative humidity RH is expressed as $\mathrm{RH_{eq}}/100 = 1 + a/R - b/R^3$. $\mathrm{RH_{eq}}$ takes its maximum at the critical radius R_c:

$$R_c(T, M) = \sqrt{\frac{3b}{a}}. \quad (2)$$

We define an unactivated aerosol particle (i.e., a haze droplet) as a droplet whose radius R is less than R_c calculated with the temperature at the position of the droplet, as in Abade et al. (2018). Eq. (1) also represents the hysteresis around the equilibrium state (Arabas and Shima 2017), which can be important for microphysical processes related to entrainment/detrainment. Collision and coalescence are approximated using a Monte Carlo scheme to reduce computational cost (Shima et al. 2009).

The SDs within a cell interact with the cell-averaged atmospheric variables by the mass, momentum, and heat conservation laws. While the SGS turbulence mixing model is used for the atmospheric flow, the SGS stochastic turbulent mixing and stochastic activation/condensation models for SDs, such as Grabowski and Abade (2017) or Abade et al. (2018), are not used in this study.

b. Experimental Setup

The basic settings of the numerical simulations, such as the computational domain size, the sounding, and how to add fluxes that initiate the isolated cumulus cloud, are based on L01 and L05. The main difference is that we spin up boundary layer turbulence before proceeding to the isolated cumulus forcing as in L01 and L05 (Grabowski 2020b).

The computational domain is $10 \times 10 \times 8\,\mathrm{km}^3$ box for the x,y, and z directions. The sounding of the SCMS field campaign on 22 July at 1545 UTC is used as the reference profile. Since the 0 °C level is at approximately 5.05 km, considering only warm-cloud processes would be appropriate if the simulated maximum cloud-top height is not much higher than this. For the lateral boundaries, doubly periodic conditions are imposed on the atmospheric variables and positions of the SDs. For the vertical direction, the Rayleigh damping is imposed above 7 km height on atmospheric variables. SDs crossing the lower boundary

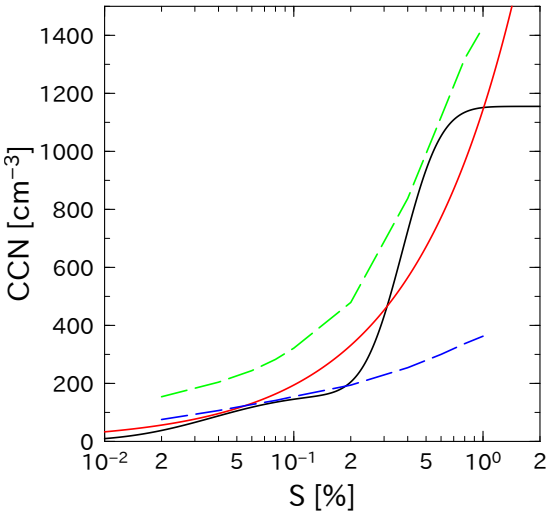

FIG. 2. Dependence of cumulative number of activated CCN on the critical supersaturation computed with fixed temperature of T = 293.15 K (black line). Green and blue dashed lines indicate the averaged CCN near cloud-base for the continental and maritime flight cases in the SCMS field campaign, respectively (plotted by Fig. 2 in Hudson and Yum 2001). Red line indicates $N = 1114.0S^{0.77}$ [cm^{-3}].

due to gravitational sedimentation are removed. Spatially uniform surface fluxes for potential temperature and water vapor are added for spin-up time, and then domain-centered Gaussian shape fluxes are added (Grabowski 2020b).

Initial conditions include a random perturbation of 0.01 K for the potential temperature and of $2.5 \times 10^{-5}\,\mathrm{kg\,kg^{-1}}$ for the specific humidity. SDs are initially randomly distributed in the physical space. The multiplicity of each SD is determined in such a way that the resulting probability density distribution of each SD is constant. We set the CCN distribution as the sum of two log-normal distributions of ammonium-bisulfate with geometric mean radii of 0.03 and 0.14 μm and geometric standard deviations of 1.28 and 1.75, respectively, as in VanZanten et al. (2011). The CCN number concentration is taken as 11 times higher than in VanZanten et al. (2011) for each mode to represent more polluted CCN conditions on that day. The number concentrations are $990\,\mathrm{cm^{-3}}$ and $165\,\mathrm{cm^{-3}}$, respectively, for the two modes. Unlike L01 and L05, we do not include any ultra-giant aerosols. Figure 2 shows the cloud base CCN spectrum, which is a function of the critical supersaturation, computed using the temperature around the cloud base, and the observed CCN spectrum. The CCN spectrum in the present setting has the intermediate properties of the maritime and continental CCN spectra, and is similar to the one used in L05.

Sensitivity simulations were conducted to investigate the impact of spatial resolution, the initial average number of SDs in a cell, and small variations in the initial conditions (i.e., applying an ensemble of simulations) on cloud dynamical and microphysical statistics. The numer-

TABLE 2. List of configurations for the numerical simulations. The columns show the case label, spatial resolution, SD number density and initial number of SDs in a cell, number of ensemble members, time interval of tracer advection (Δt) and physical process ($\Delta t_{\rm phy}$), and time interval of dynamical process ($\Delta t_{\rm dyn}$).

Case	$\Delta x = \Delta y = \Delta z$ [m]	SD density [cm^{-3}] (number of SDs)	# of ensemble members	$\Delta t = \Delta t_{\rm mphy}$ [s]	$\Delta t_{\rm dyn}$ [s]
R50-SD32	50	2.56×10^{-10} (32)	12	0.1	0.1
R25-SD32	25	2.048×10^{-9} (32)	2	0.1	0.05
R12-SD32	12.5	1.6384×10^{-8} (32)	2	0.1	0.025
R50-SD128	50	1.024×10^{-9} (128)	2	0.1	0.1
R50-SD256	50	2.048×10^{-9} (256)	2	0.1	0.1
R25-SD256	25	1.6384×10^{-8} (256)	2	0.1	0.05

ical configurations are listed in Table 2. Here, for example, the case in which resolution is 50 m and the average number of SDs per cell is 32 is denoted as R50-SD32. Assuming that convection is sufficiently resolved, we consider the spatial resolution range of 50–12.5 m. Increasing the resolution in this range improves the representation of boundary layer turbulence and thermals within a cloud. In previous studies, Sato et al. (2017, 2018) performed large-eddy simulations of the BOMEX case using the SDM and spatial resolutions within the range of 100–6.25 m. They showed that quantities related to the cloud dynamics, such as the cloud cover and the liquid water path, converge with 12.5 m, and argue that grid convergence of these quantities is achieved when the roll convection in the boundary layer becomes well resolved. Airborne radar observations (Damiani et al. 2006) showed the existence of coherent structures in clouds, thermals and vortex rings, with diameters in the range of 200–600 m. Assuming that these scales also apply in our case, and the smallest spatial scale capable of representing an eddy is 6–8 times the grid length (Skamarock 2004), coherent structures are expected to become well resolved once the grid length is in the range of 30–100 m. Even with such a high resolution, supersaturation profiles near the cloud base may remain unresolved (Grabowski and Jarecka 2015). However, since using an anisotropic grid with a higher vertical resolution distorts the nature of the turbulent flow (Nishizawa et al. 2015), an isotropic grid is used in this study.

There is no theoretical basis for setting the number of SDs to obtain converged statistics for the DSD. In Arabas and Shima (2013), sensitivity simulations using 8 to 512 SDs per grid cell have been performed for the RICO case. In Fig. 6 of that paper, the global DSD converges with 32/ cell. In Figs. 2 to 4 of that paper, however, the 45–55th percentile range of the local DSD spectral width becomes larger if the initial number of SDs exceeds 128 per cell. Hence, we take the initial number of SDs in the range of 32 to 256 per cell for the sensitivity simulations. In the case of R12-SD32, for example, the average number of droplets represented by one SD is approximately 7.05×10^{10}.

An ensemble approach is applied to investigate the uncertainty originating from the chaotic and transient behavior of cloud dynamics and microphysics. Ensemble members are generated by applying different sets of random numbers for the initial temperature and humidity perturbations as well as for the initial SD positions. Twelve ensemble members are included in the R50-SD32 simulations, while only two members are used in all the others.

The time step for cloud microphysics calculations $\Delta t_{\rm mphys}$ is chosen as smaller than the advection time scale, evaporation time scale, and phase relaxation time scale. These are estimated using the spatial resolution and the simulated CDNC and mean radius. $\Delta t_{\rm mphys}$ is also selected to ensure that its ratio to the time step in dynamics $\Delta t_{\rm dyn}$ is less than 10 (Sato et al. 2015). In each experiment, the time integration is performed for 1 hour for the spin-up to produce the boundary layer turbulence, and for another 1 hour to produce the cumulus congestus cloud. The atmospheric variables are stored every 10 seconds for the analysis. To limit disk storage, only SDs satisfying $R \geq R_c$ are stored in the same time interval.

c. *Representation of the Droplet Size Distribution*

To investigate intra-cloud microphysical spatial variability in section 4, we here introduce the DSD function and its statistics. The DSD function at (x, y, z) is expressed as the sum of the contribution of number density ξ_p/Δ^3 (ξ_p is the multiplicity and Δ is the model grid length) of each SD at (X_p, Y_p, Z_p) (p is the SD index) from all SDs:

$$f(r,x,y,z;\Delta) = \sum_p \frac{\xi_p}{\Delta^3}\delta(R_p - r)\cdot \frac{1}{h^3}K\left(\frac{X_p - x}{h}\right)K\left(\frac{Y_p - y}{h}\right)K\left(\frac{Z_p - z}{h}\right) \quad (3)$$

This formulation is based on the kernel density estimation for spatial directions, where $K(s)$ is the kernel and h is the bandwidth. For a simple treatment of the double periodic boundary condition in the horizontal direction, we extend the SD data points to the outside of the computational domain over a few grid points ($\sim h/\Delta$) by applying the periodic boundary conditions, while considering the SD

position point only in the computational domain. The kernel $K(s)$ is defined in an unbounded domain and satisfies the condition that its integral over the unbounded domain is unity. Then, the n-th moment of the DSD function is obtained by integrating the DSD with the weight r^n over cubed domain of volume Δ^3 centered at (x, y, z):

$$M_n(x,y,z;\Delta) = \int_{x-\Delta/2}^{x+\Delta/2}\int_{y-\Delta/2}^{y+\Delta/2}\int_{z-\Delta/2}^{z+\Delta/2}\int_0^\infty f(r,x',y',z')r^n dr dx' dy' dz'. \tag{4}$$

Using Eq. (4), the cloud droplet number concentration N, the integral radius I, the light extinction $\sigma_{\rm ext}$ in the geometric optics approximation, and the liquid water content L at (x, y, z) are expressed as follows:

$$N(x,y,z;\Delta) = M_0, \tag{5}$$

$$I(x,y,z;\Delta) = M_1, \tag{6}$$

$$\sigma_{ext}(x,y,z;\Delta) = 2\pi M_2, \tag{7}$$

$$L(x,y,z;\Delta) = \frac{4}{3}\pi\rho_w M_3 \tag{8}$$

where ρ_w is the density of water. Similarly, the mean radius r_m, mean volume radius r_v, the standard deviation of the radius σ_r, and k are expressed as follows:

$$r_m(x,y,z;\Delta) = M_1/M_0, \tag{9}$$

$$r_v(x,y,z;\Delta) = (M_3/M_0)^{\frac{1}{3}}, \tag{10}$$

$$\sigma_r(x,y,z;\Delta) = \sqrt{M_2/M_0 - (M_1/M_0)^2}, \tag{11}$$

$$k(x,y,z;\Delta) = M_2^3/(M_0 M_3^2). \tag{12}$$

Since Eqs. (5)–(8) are linear expressions of the moment, statistics for the cloud can be obtained by using volume averages for Eqs. (5)–(8). On the other hand, another expression is required to define the cloud statistics of Eqs. (9)–(12) since they include nonlinear moment combinations. For example, the cubed ratio of the mean volume radius to the effective radius for the cloud can be defined through the volume integral of the appropriate moments:

$$k_V = \frac{\left(\int_V M_2 dV\right)^3}{\left(\int_V M_0 dV\right)\left(\int_V M_3 dV\right)^2}. \tag{13}$$

It should be stressed that k_V is different from the volume average of k.

Kernel $K(s)$ needs to be specified to compute Eq. (3). The simplest kernel is the delta function kernel; that is, $K(s) = \delta(s)$ and $h = \Delta$. Such a kernel is used during model execution, assigning droplet properties to appropriate grid cells. However, for our analysis, we use the Epanechnikov kernel, which is a kernel with greater smoothing:

$$K(s) = \begin{cases} \frac{3}{4}\left(1-s^2\right) & |s| \le 1 \\ 0 & |s| \ge 1 \end{cases}. \tag{14}$$

Here, we chose kernel width $2h = 6\Delta$ based on validation tests which is to be described in preparing manuscript to focus on the properly resolved microphysical scale. This restricts the spatial scale for variability to a value larger than 6Δ.

4. Results

a. Validation

In order to validate the results of our numerical simulations, we investigated the sensitivity of cloud dynamical and microphysical quantities over the entire cloud to the spatial resolution, the initial number of SDs, and the initial conditions.

1) Cloud dynamics

We begin with an example of the time evolution of cloud dynamics after the spin-up process. Figure 3 shows the time evolution of the liquid water mixing ratio rendered by volume in the highest resolution R12-SD32 experiment. Since the horizontally uniform fluxes are given during the initial hour, small clouds develop sparsely above the boundary layer until $t = 3600$ s (Fig. 3a). The fluxes are then switched to have a Gaussian form, triggering strong convection. Around $t = 4800$ s, a larger cumulus cloud develops near the center of the horizontal domain (Fig. 3b). Eventually, the cumulus cloud evolves into a congestus (Fig. 3c) and reaches its maximum height around $t = 6800$ s (Fig. 3d). Between this time and the end of the integration, the cumulus is in its decaying phase. In Figs. 3c and d, the cauliflower-like structures associated with convective thermals are well resolved. Although we do not use the SGS turbulent mixing scheme for the droplets, Fig. 3d clearly shows the diluted and sparse pattern of the liquid water mixing ratio on the side wall of the cloud by detrainment. Some drizzle drops are generated during the mature and decaying phases; however, they evaporate before reaching the cloud base and are not visible in Fig. 3d.

We next document the sensitivity of cloud dynamical quantities. To find the levels where the cloud exists, we derive the cloud fraction as the ratio of the number of cloudy grid cells ($N \ge 50\,\mathrm{cm}^{-3}$) to the number of all grid cells at a given level. The bottom and top levels with the cloud fraction becoming zero define the cloud base and cloud top, respectively. Their evolutions are shown in Fig. 4a. Figure 4b shows the time evolution of the cloud cover defined as the fraction of cloudy columns in the computational domain (a cloudy column is a column with at least one cloudy grid cell). As already seen in the

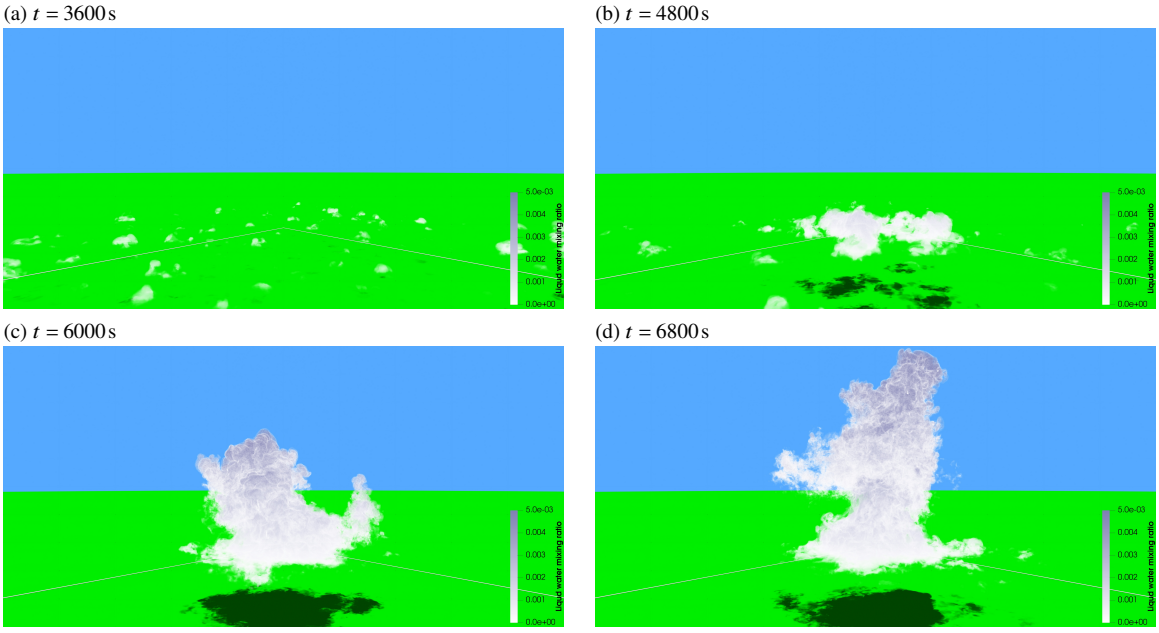

FIG. 3. Snapshots of liquid water mixing ratio field in R12-SD32 at (a) $t = 3600$ s, (b) $t = 4800$ s, (c) $t = 6000$ s and (d) $t = 6800$ s. Opacity is set as constant at 0.15 to visualize cloud dynamics on a cloud-clear air interface. The light source is positioned far above the ground from the center of the domain to visualize shadows on the ground for characterizing the cloud fraction.

R12-SD32 case, the low-level clouds first appear during the spin-up process during $0\,\text{s} \le t \le 3600\,\text{s}$ for each case (Fig. 4a). The cloud-top height of the low-level clouds is similar for each case, but the cloud cover is different. In the simulations with 50 m grid length, the cloud cover reaches a maximum of around 0.1 for t around 3400 s, and then decreases to below 0.02 at $t \sim 4500$ s. However, in simulations with horizontal resolutions higher than 25 m, the cloud covers gradually increase until $t \sim 4200$ s (Fig. 4b). The unique behavior of the cloud cover in the 50 m grid length cases originates from a delay in the turbulence development during the first hour spin-up and an increase of water vapor near the boundary layer top triggering strong water vapor flux for a short time (not shown). During $3600\,\text{s} < t < 4800\,\text{s}$, the cumulus clouds near the center of the horizontal domain evolve gradually (Fig. 4a). The cloud cover tends to increase as the resolution increases (Fig. 4b). As time progresses ($t > 4800$ s), the cumulus clouds evolve into a single large cumulus congestus cloud (Fig. 4a). The cloud cover increases monotonically with time, and the differences between various spatial resolutions arguably reflect different flow realizations (Fig. 4b). The same applies to other cloud properties shown in Fig. 4. Since the maximum cloud-top heights in the L01 and L05 simulations and in the observations are within the range of 5000–5350 m, the results of this study agree well with previous investigations. It takes approximately 20–35 minutes for the cloud top to increase from 2000 m to its maximum height, which is slower than in the previous studies. However, since the spin-up process is different from that in L01 and L05, one might expect that the time required for the cloud to reach its maximum vertical extent is different.

Figure 4c shows the time series of the volume-averaged LWC for the cloudy grid cells. Since the cloud-top height (Fig. 4a), as well as the volume-averaged LWC (Fig. 4c), fluctuates significantly in each experiment, the ensemble means of the time-and volume-averaged LWC for the period between $t = 6000$ s and 7200 s for each case are also shown in the right panel of Fig. 4c. The variation of the time- and volume-averaged LWC is approximately 1.1–1.4 g m^{-3}. Since the ensemble means of the time-averaged LWC for each case are within the variability range of the R50-SD32 ensemble, the impact of the spatial resolution and SDs number is not clear. Figure 4d shows the time series of the 99.5th percentile LWC for the cloudy grid cell, together with the time-averaged ensemble means. The ensemble means are approximately 5 g m^{-3} and are consistent with the maximum value of the LWC in L01 and L05 ($> 5\,\text{g m}^{-3}$). In Fig. 4d, the ensemble means of the time-averaged 99.5th percentile LWC for each SD32 case are within the variability range of the R50-SD32 ensemble. However, the R50-SD128 and R50-SD256 ensemble means are not within the variability range of the R50-SD32 ensemble, and the range tends to decrease as the number of SDs increases. Since the variability range for the R50-SD32 ensemble and the difference between the ensemble mean for R50-SD128 and R50-SD256 cases are approxi-

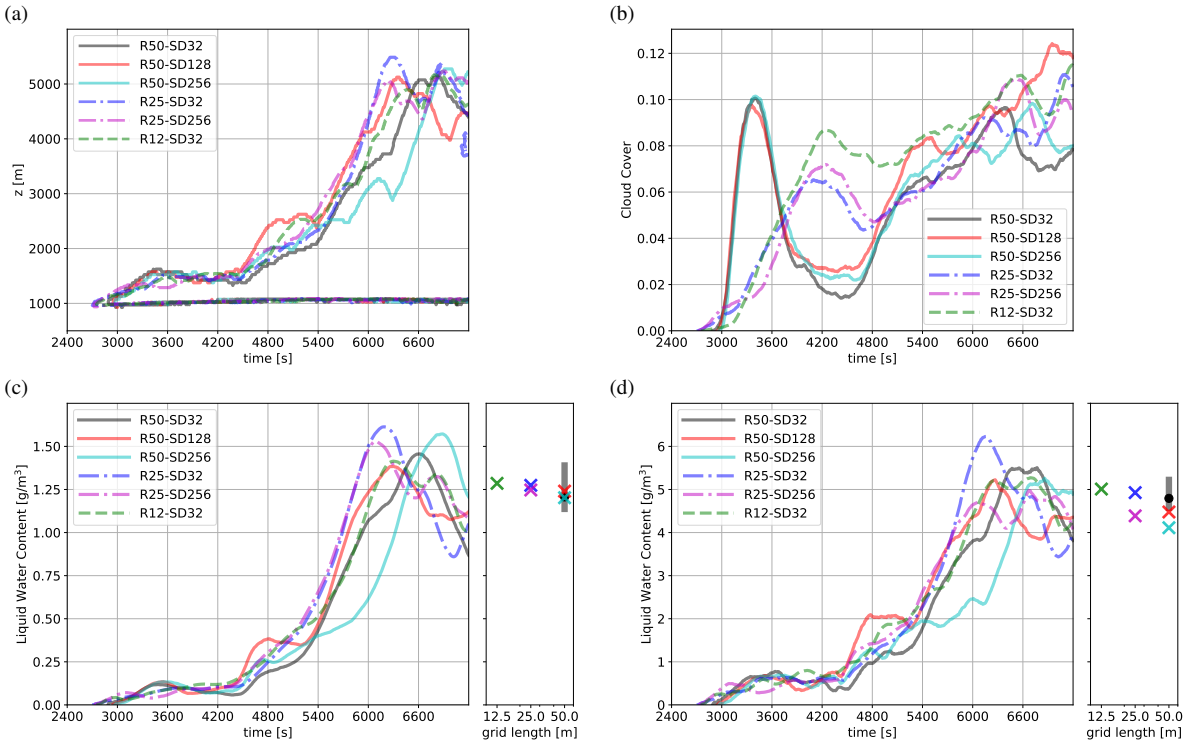

FIG. 4. Time evolutions of (a) cloud-base height and cloud-top height, (b) cloud cover, (c) volume mean LWC (left panel), and (d) 99.5th percentile LWC (left panel) for one member from each configuration. Ensemble mean, minimum, and maximum of the time-averaged statistics from $t = 6000\,\mathrm{s}$ to $7200\,\mathrm{s}$ for each configuration are shown in right panel of (c) and (d). Vertical lines show the minimum to maximum range of the ensembles. Filled circles and crosses indicate ensemble means.

mately the same, it can be argued that the time-averaged 99.5th percentile LWC is converged with 128 SDs per cell.

2) CLOUD MICROPHYSICS

The microphysical sensitivity of the simulated cloud can be assessed using the moments of the DSD and k. Figure 5a shows the time series of the volume-averaged CDNC for the cloudy grid cell. During the developing phase of the cumulus congestus cloud ($4200\,\mathrm{s} < t < 6000\,\mathrm{s}$), the volume-averaged CDNC tends to increase significantly in each simulation, while the temporal changes during $2400\,\mathrm{s} < t < 5400\,\mathrm{s}$ and $6000\,\mathrm{s} < t < 7200\,\mathrm{s}$ are relatively small. The ensemble means of the time- and volume-averaged CDNC for the period from $t = 6000\,\mathrm{s}$ to $7200\,\mathrm{s}$ are also shown in Fig. 5a. In each simulation, the volume-averaged CDNC changes moderately with time, and the variation of the time- and volume-averaged CDNC is small. For instance, the variability range for the R50-SD32 ensemble is approximately $30\,\mathrm{cm}^{-3}$. The ensemble mean of the time- and volume-averaged CDNC tends to decrease as the number of SDs increases. Since the CDNC variability range of the R50-SD32 ensemble and the difference between ensemble means for the R50-SD128 and R50-SD256 ensembles are approximately the same, it can be argued that the time- and volume-averaged CDNC is converged with 128 SDs per cell. On the other hand, the ensemble mean of the time- and volume-averaged CDNC tends to increase as the spatial resolution increases, and it is not converged with the grid length down to 12.5 m.

Figure 5b shows the time series of the volume-averaged integral radius for the cloudy grid cells and ensemble means of the time- and volume-averaged integral radius for each case. The variability range of the time- and volume-averaged integral radius for R50-SD32 is approximately $500\,\mathrm{m}^{-2}$. The ensemble of time- and volume-averaged integral radius tends to decrease as the number of SDs increases, and it tends to increase as the spatial resolution increases. The differences of the ensemble mean of the time- and volume-averaged integral radius between R50-SD128 and R50-SD256 and between R25-SD32 and R12-SD32 are smaller than the variability range of the R50-SD32 ensemble. Thus, it seems that the time- and volume-averaged integral radius is converged with 25 m and 128 SDs per cell. Figure 5c shows the time series of the volume-averaged light extinction for the cloudy grid cells. Since the difference of the time- and volume-averaged light extinction between R50-SD128 and R50-SD256 is smaller than the variability for the R50-SD32 ensemble, it can be argued again that the time- and volume-averaged light extinction

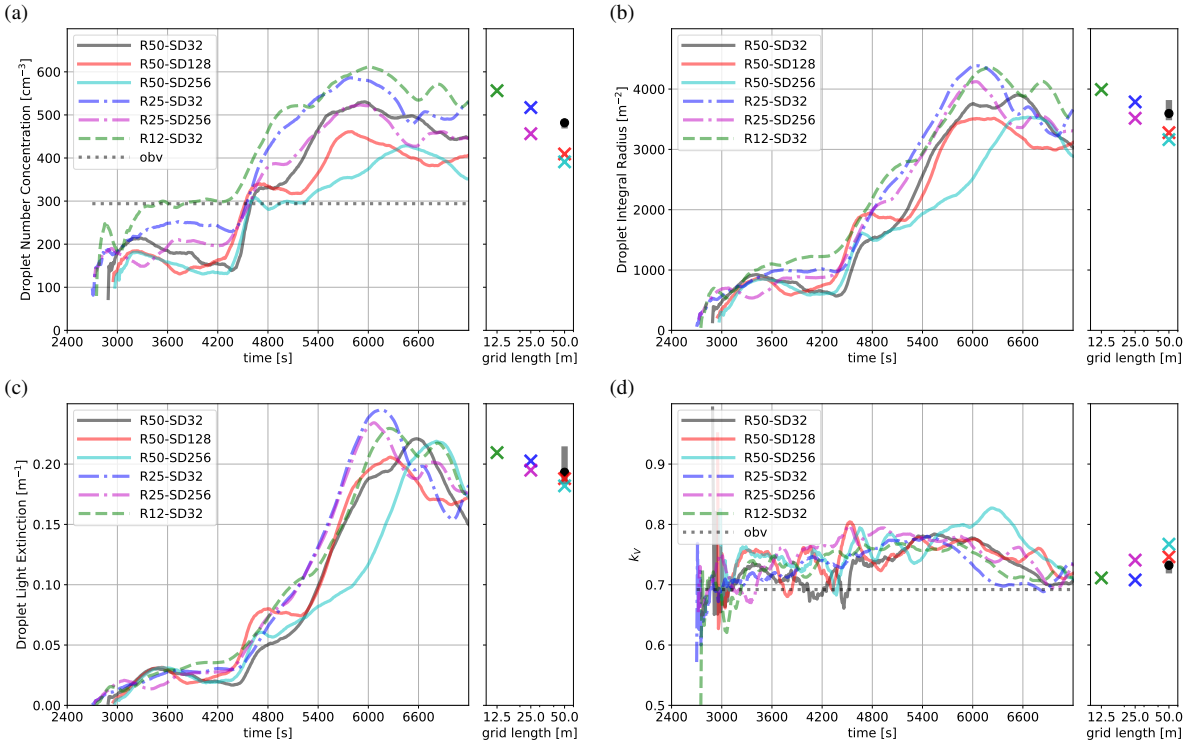

FIG. 5. Time evolutions of (a) the volume mean CDNC, (b) the volume mean integral radius, (c) the volume mean light extinction, and (d) the k_V for one member from each configuration. Ensemble mean, minimum, and maximum of the time-averaged statistics from $t = 6000$ s to 7200 s for each configuration are shown in the right panel. The vertical lines show the minimum to maximum ranges of the ensembles. Filled circles and crosses indicate ensemble means.

is also converged with 128 SDs per cell. The ensemble means of the time- and volume-averaged light extinction are within the variability range of the R50-SD32 ensemble. From these results, it appears that the lower the order of the DSD moment, the smaller the variation within the ensembles, and the higher the order of the DSD moment, the smaller the sensitivity to the spatial resolution and the number of SDs.

We next compare the cloud microphysical quantities from the sensitivity simulations with the observations. As shown in Table 1, observations of the average and variability range of the local CDNC are available. Because the DSD moments averaged over the entire cloud involve volume integrals similar to Eq. 4, the simulated volume-averaged moments can be compared with the average moments obtained locally in the observations. However, the statistics obtained from the observations are for the cloud observed at different times. In Fig. 5a, the CDNC tends to be larger than the observed CDNC for $t > 4800$ s. The difference between the time- and volume-averaged CDNC for R50-SD128, R50-SD256, and R25-SD256, and the observed CDNC is approximately 150 cm^{-3}. Such a difference may be considered large. However, since the CCN number concentration in L05 and in this study has a difference of up to 300 cm^{-3} at critical supersaturation smaller than 1% (Fig. 2), it follows that the difference between the ensemble mean of the time- and volume-averaged CDNC and the observed CDNC is within the uncertainty range. Figure 5d shows k_V for the cloudy grid cells and the ensemble means of the time-averaged k_V. Since the k_V becomes identical to k^* if the cloud is vertically uniform, k_V can be roughly compared with k^*. The k_V does not fluctuate much over time and generally takes a value around $k_V = 0.75$. The ensemble mean of the time-averaged k_V tends to decrease as the spatial resolution increases, and it increases as the number of SDs increases. This implies that the impact of CDNC in the denominator of Eq. (13) has the largest impact on k_V. Although the ensemble means of the time-averaged k_V for each ensemble are larger than the value $k^* = 0.692$ obtained in the 22 July observations, it is about the same as the mean value of $k^* = 0.753$ simulated with grid lengths equal to or smaller than 25 m.

b. Intra-cloud microphysical variability

Based on the results of the sensitivity simulations in section 4a, we selected a proper experiment to investigate the cloud microphysical variability related to turbulent eddies. For this purpose, we chose an experiment with relatively good convergence for the average characteristics of cloud

dynamics and microphysics (LWC, CDNC, r_v), a measure of cloud water dilution (AF), and an index related to the DSD (k). Because LWC has little dependence on the spatial resolution and is converged with 128 SDs per cell, it is sufficient to take 128 SDs per cell for LWC and AF. Although the CDNC and light extinction are not converged with a grid length down to 12.5 m, they are converged with 128/ cell. For this reason, statistical error and bias for the CDNC, r_v, and k are reduced if the initial number of SDs is 128 per cell or more. Thus, we use a simulation from the R25-SD256 set that has a statistically sufficient number of SDs and a relatively high spatial resolution.

1) Spatial variability

We first investigate the spatial fluctuations of the cloud microphysics. Since cloud dynamics is transient, we use snapshots of the R25-SD256 simulation for the developing ($t = 6000$ s), maturing ($t = 6240$ s), and decaying ($t = 6480$ s) stages. To show the average characteristics together with quantities related to dilution, we introduce a transfer function that projects the variables onto the HSL (hue/saturation/lightness) color space. For a quantity representing the average characteristics of cloud microphysics, we select the LWC and project r_v onto the hue space. Because the lightness and saturation affect the image of dilution, we project AF onto the lightness space and k onto the lightness and saturation space. With such a projection, LWC and AF, or r_v and k, can be represented as a single figure. Figure 6 shows snapshots of the LWC-AF, CDNC/N_a, and r_v-k. For a later comparison with the observations, water droplets with diameters only in the range of 5.2–38.4 μm, corresponding to the Fast-FSSP range, are used to compute cloud microphysical quantities. The AF is computed using the local LWC and adiabatic LWC, where the adiabatic LWC is defined as the LWC of an air parcel lifted by a reversible adiabatic process from $z = 1000$ m near the cloud base. The initial parcel temperature and water vapor mixing ratio are taken as horizontally weighted averages of the model output, with the weight proportional to $\exp(-4r^2/\sigma_F^2)$, where r is a horizontal distance from center of the domain and $\sigma_F = 1700$ m. Finally, the cloud base adiabatic droplet concentration N_a is selected as $1000\,\mathrm{cm}^{-3}$. Note that, in contrast to AF, the CDNC within the adiabatic parcel depends at the assumed parcel's updraft speed when crossing the cloud base. This is because the updraft, together with CCN characteristics, determines the maximum supersaturation the parcel reaches near the cloud base and thus the separation between activated and unactivated CCN. The adiabatic CDNC N_a was selected based on the maximum CDNC at the cloud base in the numerical simulations presented here.

Figure 6a shows that the LWC at the cloud core increases with height for $z < 2500$ m. There is a large spatial variation and dilution of LWC due to entrainment for $z > 2500$ m. Figure 6a also shows AF spatial variations corresponding to the dilution of LWC. For example, the AF is large at $(x, z) = (5000, 2000)$ m at the cloud core, whereas it is small at $(x, z) = (5500, 2000)$ m at the cloud side wall and also small at $(x, z) = (5000, 3500)$ m in the upper part of the cloud. Figure 6b documents large spatial variations of the CDNC. The CDNC reaches its maximum at the cloud core above the cloud base where the updraft is the strongest. In addition to large spatial fluctuations at the side wall and in the upper layers of the cloud, Fig. 6b also shows that there is spatial variation at the cloud core due to turbulent fluctuations. The reduction of the CDNC against its adiabatic prediction N_a is mainly at the side wall of the cloud. Figure 6c shows that r_v increases with height for $z < 2500$ m with large spatial variations near the side wall and for $z > 2500$ m. Figure 6c shows that k is large in the middle of the cloud core and is reduced for $z > 2500$ m.

The dilution pattern of the LWC and CDNC affects the variability of k and r_v as shown in Fig. 6. For instance, in the nearly adiabatic cloud core where the AF is large (e.g., at $(x, z) = (5000, 2000)$ m), k is large as well. On the other hand, near the cloud side wall and at the upper cloud layers where AF is small (e.g., at $(x, z) = (5500, 2000)$, and $(5000, 3500)$ m, respectively), k is also small. This suggests that the spatial patterns of AF and k are positively correlated. In addition, r_v decreases with decreasing CDNC at $z = 2500$, while r_v does not decrease substantially with decreasing CDNC at $z = 4000$. These patterns between the CDNC and r_v show qualitative differences of mixing-induced variability depending on the location.

2) Frequency analysis

To investigate the evolution of cloud microphysical variations, Fig. 7 shows profiles of the AF, CDNC, and k frequency distributions. In the lowest kilometer of the cloud depth, the maximum AF frequency distribution is close to 1 and the mean is around 0.6. Although AF frequencies close to 1 are small in the upper layers, there exist cloudy grid cells with relatively small cloud water dilutions (AF$\sim$ 0.975). AF has modes (i.e., local peaks) close to 0 that are in response to the dilution caused by entrainment. The frequency of the modes near 0 increases as the cloud evolves towards the decaying stage ($t = 6480$ s). The mean AF decreases with height, in agreement with numerous previous shallow and congestus cumulus observations, starting with Warner (1955). As time progresses ($t = 6240$ and 6480 s), entrainment leads to a decrease in AF, and AF fluctuates between 0.2 and 0.4 above $z > 2500$ m.

An adiabatic CDNC that decreases from the cloud base due to the expansion of rising air parcels is also shown in Fig. 7. The maximum CDNC agrees well with the adiabatic value. The distribution of CDNC has a mode around 600–800 cm^{-3} and a mode around 50 cm^{-3} that comes from entrainment. (Note that cloudy grid cells with

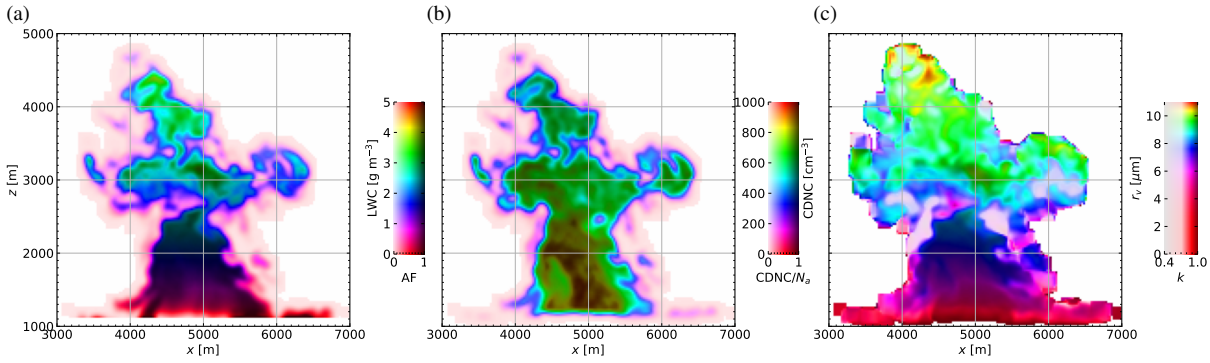

FIG. 6. Snapshots of the (a) LWC-AF, (b) CDNC-CDNC/N_a, and (c) r_v-k on the plane $y = 5000$ m at $t = 6240$ s for the R25-SD256 case. Here, N_a is an adiabatic prediction of the CDNC defined as $1000\overline{\rho}(z)/\overline{\rho}(z_{\mathrm{cbase}})$ [cm^{-3}], where $\overline{\rho}$ is the horizontally averaged total density profile and z_{cbase} is the cloud base height.

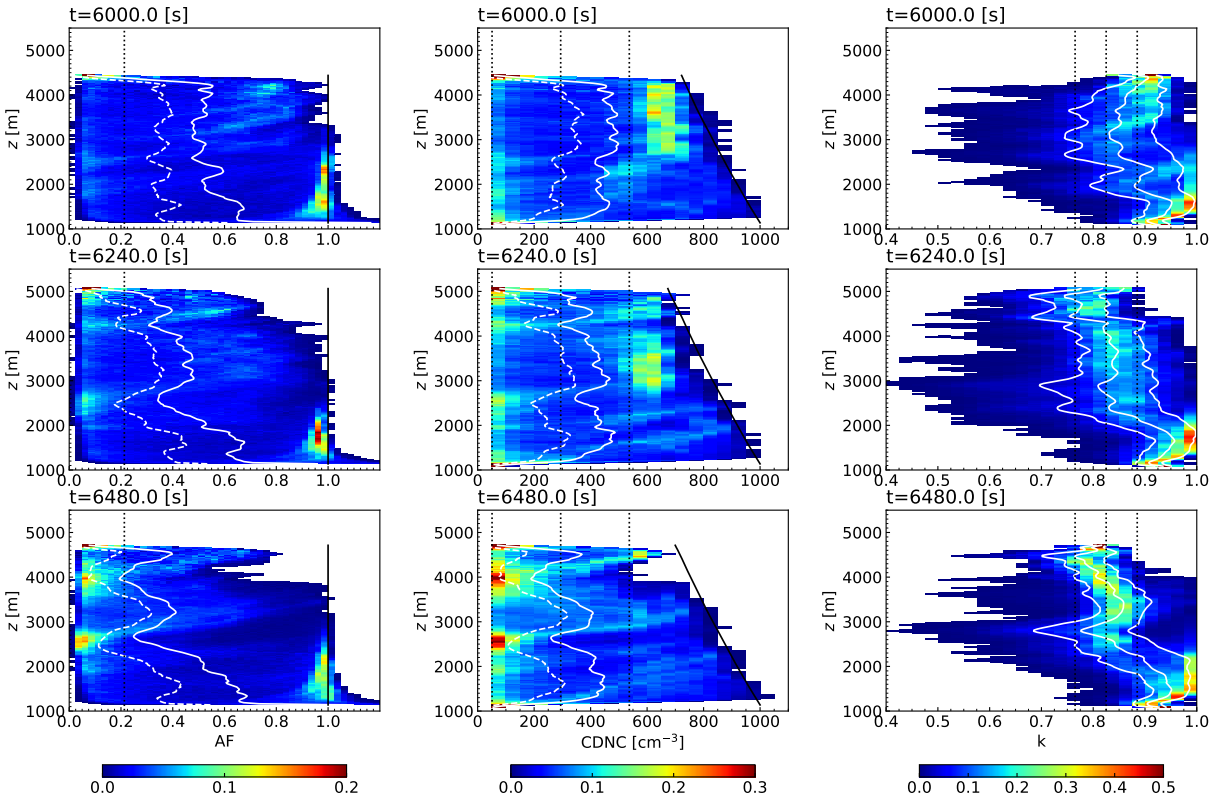

FIG. 7. Frequency distributions of the AF, CDNC, and k for $t = 6000$ s, $t = 6240$ s and $t = 6480$ s. Distributions are normalized so that the integral of frequency at each height level is 1. Bin sizes for AF, CDNC, and k are 0.025, 50 cm^{-3}, and 0.025, respectively. The white solid and dashed lines in the AF and CDNC panels at each time show the mean values calculated using the cloudy grid cells ($N > 50$ cm^{-3}) and grid cells ($N > 0$ cm^{-3}), respectively. The black solid lines in the AF and CDNC panels show the adiabatic prediction of the AF and CDNC (N_a). The white solid lines in the k panel show the mean values and the mean plus/minus standard deviation values calculated using the activated droplets that lie in the Fast-FSSP measurement range. The black dotted lines in each panel show AF = 0.213, CDNC = 294 ± 243 cm^{-3}, and $k = 0.0825 \pm 0.060$.

$N < 50$ cm^{-3} are not used in the frequency distribution analysis.) Similarly to the AF, frequencies around $N = 50$ cm^{-3} increase as the cloud evolves. The horizontal CDNC average is nearly constant with height.

The distribution of k has a mode close to 1 in the lowest kilometer of the cloud depth. In the upper layers of the cloud, the distribution of k has a maximum around 0.8–0.9. This agrees with the spatial variation pattern of k shown in Fig. 6c. The horizontal average of k in the cloud

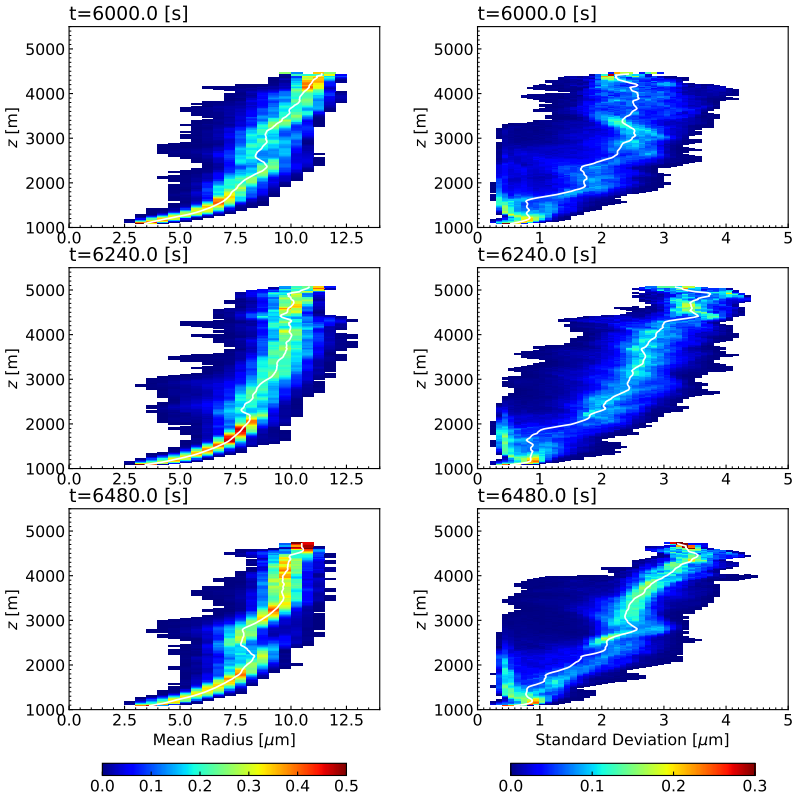

FIG. 8. Frequency distributions of the radius mean and standard deviation for $t = 6000\,\mathrm{s}$, $t = 6240\,\mathrm{s}$, and $t = 6480\,\mathrm{s}$. The distributions are normalized so that the integral of the frequency at each height level is 1. Bin sizes for the radius mean and standard deviation are $0.5\,\mu\mathrm{m}$ and $0.1\,\mu\mathrm{m}$, respectively. The white solid lines in each panel show the medians of the frequency distributions.

tends to decreases above $z > 2500\,\mathrm{m}$ and oscillate within 0.76–0.92.

As mentioned in section 2, AF, CDNC, and k have reference values obtained from observation (see Table 1). These are plotted as black dotted lines in Fig. 7. We can compare the mean and variability of the microphysical variables with the observations statistically. To compute the mean values at each height level, we need to set a threshold value to eliminate small CDNC cloudy samples. This is because cloudy cells may not contain a sufficient number of SDs to compute spectral width (Arabas et al. 2009). In Arabas et al. (2009) and Arabas and Shima (2013), a threshold $N = 20\,\mathrm{cm}^{-3}$ was set. In this case, since the number of the droplets comprising an SD isapproximately 11 times larger than Arabas and Shima (2013), we should use a larger threshold than is used in their study to roughly match the number of SDs in a cell. We set a threshold of $N = 50\,\mathrm{cm}^{-3}$ and compared the mean values of AF, CDNC, and k with the observations. However, since the distributions of AF and CDNC for each height level are not normal distributions and the frequency of the modes around 0 is relatively high, the mean values of AF and CDNC would appear to be sensitive to the threshold. For this reason, as a reference for the sensitivity of the mean values, we also show the mean values of AF and CDNC using a threshold of $N = 0\,\mathrm{cm}^{-3}$. The mean values of AF are larger than the observed value at $t = 6000\,\mathrm{s}$, but agree well with the observed values at $t = 6240\,\mathrm{s}$ and $t = 6480\,\mathrm{s}$ and $z \sim 2500\,\mathrm{m}$ and $z \sim 4000\,\mathrm{m}$. The mean values of the CDNC also are in good agreement with the mean value of the observation at $t = 6240, 6480\,\mathrm{s}$ and $z \sim 2500, 4000\,\mathrm{m}$. The mean values of k in the clouds agree fairly well with the observation above $z > 2500\,\mathrm{m}$ during $6000\,\mathrm{s} < t < 6480\,\mathrm{s}$. Moreover, the mean values of k plus/minus standard deviations are in good agreement with observation above $z > 2500\,\mathrm{m}$. Although our results do not yet reach grid convergence, the fact that the simulated AF, CDNC, and k agree with the observations encourages some confidence in the simulated droplet spectra.

For the DSD statistics, Fig. 8 shows frequency distributions of the mean radius r_m and the droplet radius standard deviation. The mean radius r_m increases with height and its distribution is relatively narrow in the lowest kilometer or so. The distribution broadens due to entrainment above $z > 2500\,\mathrm{m}$. The distribution of the droplet standard deviation has two modes in the lowest cloud layers, one that decreases with height and one that increases with height from around 1 μm just above the cloud base. The mode that

decreases with height likely represents the classical narrowing of the droplet spectrum due to the parabolic droplet growth (i.e., larger droplets increasing their radius slower compared to the smaller droplets). This corresponds to the mode of the k distribution that increases with height just above the cloud base as shown in Fig. 7. In the upper layers, the averaged standard deviation increases with height, reaching values from 3 to 4 μm at $t = 6240, 6480$ s.

3) Microphysics – entrainment relation

In order to investigate the relation between the microphysical variables and cloud dilution for the resolved scale, Fig. 9 shows a two-dimensional probability density function of AF-k at $t = 6480$ s. There are two modes evident in the diagram: one at $(\mathrm{AF}, k) \sim (0.05, 0.825)$ and one at $(\mathrm{AF}, k) \sim (0.975, 0.975)$. The first mode corresponds to cloudy volumes near the cloud edge where the cloud is strongly diluted by entrainment. The second mode corresponds to the region of the adiabatic core where AF and k are large, as shown in Fig. 6. To investigate whether the variation of k can be predicted by AF, we perform a quantile regression (Koenker and Bassett Jr 1978). The τ-th quantile regression is obtained by minimizing the sum of the sample loss function $\rho_\tau(y) = (\tau - \mathbf{1}_{y<0})y$, referred to as the tilted absolute value function, where $\tau \in (0, 1)$, y is the sample error, and $\mathbf{1}_{y<0}$ is the indicator function equal to 1 if $y < 0$ and 0 otherwise. Quantile regression has advantages over the least squares method in that it does not assume a normal distribution for the errors, and it is more robust and flexible for prediction. Figure 9 also shows a quantile regression for k, the predictor variable, applying AF as the explanatory variable. The 0.5 quantile regression is approximated as $k = 0.176\mathrm{AF} + 0.798$. The slopes of the 0.25 and 0.75 quantile regressions are nearly the same as for the $\tau = 0.5$ case; the intercepts differ by approximately 0.05. Since the 0.25–0.75 quantile regressions cover a large probability region when AF < 0.4, the decrease of k related to spectral broadening is well explained by the decrease of AF associated with entrainment. The slope of the quantile regression decreases as τ increases. The width between the 0.1 and 0.9 quantile regressions for AF = 1 is approximately 0.075, while the width for AF = 0 is about 0.2. Thus, the prediction of k by AF becomes more uncertain as AF decreases.

Figure 10 shows the two-dimensional probability density function of the simulated CDNC and mean volume radius relative to their adiabatic values. The diagram was originally proposed by Burnet and Brenguier (2007) and is referred to as a mixing diagram. Since mixing regimes can be inferred from the variability of the CDNC and r_v using a mixing diagram, this type of diagram has been used in observational (Lehmann et al. 2009) and modeling studies (Jarecka et al. 2013). In Fig. 10, the extremely inhomogeneous mixing regime is characterized as $r_v^3/r_{va}^3 = 1$ because fast droplet evaporation at the cloud – clear air interfaces during turbulent stirring reduces the droplet number concentrations, keeping the mean volume radius unchanged. The homogeneous mixing regime is theoretically predicted as follows: Environmental dry air is entrained by thermals that have a cauliflower-like structure, as shown in Fig. 3. We assume that the source of the entrained dry air is the lateral interface of the clouds at $z > 2500$ m, where the dilution of cloud water is apparent in Fig. 6 and Fig. 7, and consider mixing between the adiabatic parcel and only a one-point source from the environment. We linearly mix the CDNC, equivalent potential temperature, and cloud water mixing ratio computed by the adiabatic parcel model with those from the environment at the same height, applying a range of mixing fractions, and evaporate cloud water until saturation conditions are met. The decrease of r_v is computed using the environmental air mixing fraction and the diluted LWC. In Fig. 10, the homogeneous mixing regime is shown for $z = 3500$ m and environmental dry air of RH = 65%.

The probability density lies in the region where AF ≤ 1 and $\mathrm{CDNC}/N_a \leq 1$ with reference to the adiabatically predicted value ($\mathrm{AF} = \mathrm{CDNC}/N_a = r_v^3/r_{va}^3 = 1$). However, r_v is not restricted by the adiabatic predictions and extends to $r_v^3/r_{va}^3 > 1$. This is because the adiabatic CDNC, N_a, is not uniquely determined, as mentioned previously. In fact, in the observations discussed in Burnet and Brenguier (2007), N_a was assumed to be the highest droplet concentration observed at the cloud penetration level. Here, we assume N_a is equal to 1000 cm^{-3} at the cloud base and adjust it to the analysis height, as shown by the solid black lines in the middle panels of Fig. 7. The area surrounded by white lines along AF ~ 0.9 corresponds to the spatial variations of the nearly adiabatic core of the cloud, with the CDNC varying due to the cloud base updraft strength affecting CCN activation (see the middle panel of Fig. 6). With a CDNC lower than N_a, the ratio r_v^3/r_{va}^3 reaches values larger than 1. The portion of the diagram showing the strong impact of entrainment is enclosed by the magenta line (25% highest frequency region), with the maximum near $(\mathrm{CDNC}/N_a, r_v^3/r_{va}^3) \sim (0.1, 0.6)$. The 25% highest frequency region represents a combination of either an inhomogeneous or homogeneous mixing line starting at around $\mathrm{CDNC}/N_a \sim 0.7$.

The spatial scales of the entrainment-mixing events resolved in model simulations (~ 150 m) are an order of magnitude larger than the droplet statistics observed by the Fast-FSSP. However, a rough comparison between model results and typical observations is possible. The pattern for AF-k in Fig. 9 qualitatively agrees with the observational study by Brenguier et al. (2011) that shows a positive correlation between the AF and k for cumulus observed on 6 August in the SCMS field campaign. The 25% highest frequency region for CDNC/N_a-r_v^3/r_{va}^3 in Fig. 9 also agrees relatively well with Fig. 8b and 8c in Burnet and Brenguier

(2007), which show mixing diagrams for observations on 6 and 10 August in the SCMS field campaign.

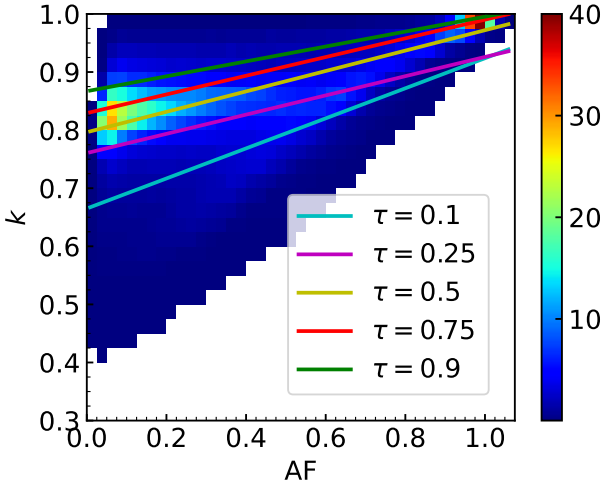

FIG. 9. Two-dimensional probability density function for the adiabatic fraction AF and k for cloudy grid cells ($N > 50\,\mathrm{cm}^{-3}$) above $z > 1500\,\mathrm{m}$ at $t = 6480\,\mathrm{s}$ in R25-SD256. The cyan, magenta, yellow, red, and green lines show quantile regressions for objective variable k and predicted variable AF, with quantiles $\tau = 0.1, 0.25, 0.5, 0.75$, and 0.9, respectively.

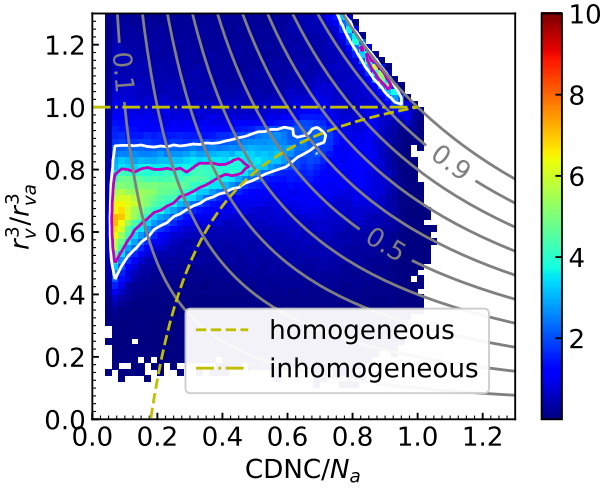

FIG. 10. Two-dimensional probability density function for the CDNC and cubed volume mean radius relative to their adiabatic value (r_{va} and N_a, respectively) for cloudy grid cells ($N > 50\,\mathrm{cm}^{-3}$) above $z > 1500\,\mathrm{m}$ at $t = 6480\,\mathrm{s}$ in R25-SD256. $N_a(z) = 1000\overline{\rho}(z)/\overline{\rho}(z_{\mathrm{cbase}})$ [cm^{-3}], where $\overline{\rho}$ is the horizontally averaged total density profile and z_{cbase} is a cloud base height. The gray contour lines of the AF (the product of r_v^3/r_{va}^3 and CDNC/N_a) are plotted by 0.1 interval for reference. The areas surrounded by a magenta/white line are the 25%/50% highest frequency regions. The homogeneous/inhomogeneous mixing line is plotted as a yellow dashed/dotted-dashed line.

5. Discussion

In this study, we investigated microphysical variability at the $\sim 100\,\mathrm{m}$ spatial scale. Because the microphysical observations of the SCMS field campaign were performed at the $\sim 10\,\mathrm{m}$ scale (i.e., 10 Hz data for an aircraft flying at a speed of approximately $100\,\mathrm{ms}^{-1}$), there is still a scale gap between our numerical simulations and the observations. The reason for selecting a spatial scale of 6Δ in contrast to previous studies that applied Δ such as Arabas and Shima (2013) is based on the dynamics of effective resolution. Some of the aspects of higher resolution simulations are discussed below.

The convergence of cloud microphysical quantities based on the sensitivity simulations is one of the aspects meriting discussion. Our results show that the sensitivity to the spatial resolution and to the initial number of SDs for the n-th DSD moment increases as n becomes small. We also remind the reader that the contribution of the n-th moment for an SD in Eqs. (3) and (4) is approximated as $\xi/\Delta^3 R^n$. From these considerations, we can assume that the major contribution of the sensitivity and ensemble variance of the mean characteristics of the n-th DSD moment is ξ and R, respectively, and the variance becomes larger as non-positive integer n becomes larger. Since Grabowski and Jarecka (2015) showed that the CDNC converges at a grid length of several meters, we estimate that grid convergence of all DSD moments, i.e., the global DSD, will be reached at a grid length of several meters.

The second aspect relates to the entrainment-mixing regime for the set of R25-SD256 simulations. The mixing regime is considered to be determined by the ratio of two time scales, the eddy-turnover time scale and the microphysical reaction time scale, the latter being either the droplet evaporation time scale or the phase relaxation time scale. (See, for instance, Lehmann et al. (2009).) We estimate these time scales since they are critical for the variability shown in Fig. 10. Eddy turnover time scale $\tau_{\mathrm{eddy}} = (L^2/\epsilon)^{1/3}$ (L: length scale, ϵ: eddy dissipation rate) for R25-SD256 is estimated as $\tau_{\mathrm{eddy}} = 282\,\mathrm{s}$ for $L = 150\,\mathrm{m}$ and $\epsilon = 0.001\,\mathrm{m}^2\mathrm{s}^{-3}$. The evaporation time scale $\tau_{\mathrm{evap}} \equiv R\left(\frac{dR}{dt}\right)^{-1}$ for RH = 65% and $R = 10\,\mu\mathrm{m}$ at $z = 3500\,\mathrm{m}$ is estimated as $\tau_{\mathrm{evap}} \sim 2.5\,\mathrm{s}$. Finally, the phase relaxation time scale in R25-SD256 is estimated as approximately 1 s for the time- and volume averaged-integral radius of approximately $3500\,\mathrm{m}^{-2}$. Since the evaporation and phase relaxation time scales are much smaller than the eddy turnover time scale, mixing for the 150 m scale is estimated to be inhomogeneous. Indeed, Fig. 10 shows that the variability of r_v/r_{va} is small, while the variability of CDNC/N_a is large, which suggests that entrained dry air does not affect droplets inside clouds, while droplets near the cloud interface evaporate.

The eddy turnover time does not fall below the evaporation and phase relaxation time scale unless the spatial

resolution is reduced to sub-meter scales and/or the turbulence intensity is much larger than assumed here. However, the simulated mixing regime is expected to be robust for spatial resolutions in the 10 m–100 m range even for extreme turbulence intensities. In addition, although the DSD numerical convergence with respect to the spatial resolution is not reached with 12.5 m grid length, some of the obtained results, such as k above the middle cloud layers, agree reasonably well with the observations. For that reason, important features of the large-scale variability driven by entrainment and mixing in the simulated cloud are qualitatively well represented.

In this study, we did not investigate the resolution dependence of the microphysical parameters or their spatial variability. Such study is left for future work, as it is important to understand the advantages of the SDM over conventional bulk and bin models. Although we did not discuss the kernel averaging method in this paper, preliminary results show that k is positively biased without the kernel (i.e., when calculating k at the grid scale), and some averaging is important to correct the positive bias. Details of these results will be reported in the future.

6. Summary

The purpose of this study was to investigate the intra-cloud variability of the DSD statistics at spatial scales resolved by large-eddy simulations applying the super-droplet method (SDM) and targeting the isolated cumulus congestus cloud observed in the 1995 SCMS field campaign (Lasher-Trapp et al. 2001, 2005). We first investigated the sensitivity of cloud dynamical and microphysical quantities to the spatial resolution, the initial average number of SDs in a cell, and the initial conditions. Cloud dynamical quantities such as the cloud top and cloud base height and LWC were not sensitive to the spatial resolution and initial average number of droplets in a cell, although the behavior of the boundary layer clouds during the spin-up period was different when a 50 m horizontal grid length was applied as compared to higher resolution simulations. For the DSD moments, the variation between ensembles was smaller for moments of a smaller order. In contrast, sensitivity to the spatial resolution and to the initial number of SDs in a cell was larger for moments of a smaller order. The time- and volume-averaged LWC and CDNC are converged with an initial average SD number of 128 per cell, and LWC and extinction factor are converged with a grid length of 12.5 m. We also attempted to validate the simulated cloud system statistics by comparing them to observations. The time- and volume-averaged CDNC and time-averaged k_v were larger than observed; however, the errors of the CDNC were within the uncertainty bounds of the initial CCN concentrations.

Based on the sensitivity analysis, the intra-cloud microphysics variability was investigated for one of the simulations with 25 m grid length and 256 SDs per cell (i.e., from the R25-SD256 ensemble). That ensemble was considered to be the most appropriate from the numerical convergence point of view. The distributions of AF and CDNC have one mode (i.e., a local maximum) around the adiabatic values and a second mode around small values in response to the dilution by entrainment. The cubed ratio of the mean volume radius and the effective radius, k, is distributed around 0.8–0.9 in the upper cloud layers. We compared the mean values of AF, CDNC, and k with observation using cloudy samples where CDNC $> 50\text{cm}^{-3}$. As a result, the mean values of AF and CDNC agreed well with observations above $z > 2500$ m in the maturing and decaying stages of the clouds. Moreover, the mean values of k and its standard deviation agreed fairly well with observations. These results provide a degree of reliability for the dynamically constrained DSD in our simulations. For the impact of entrainment on the DSD statistics, the mean radius distributions were broadened above $z > 2500$ m, and the mean radius standard deviation was 3–4 μm in the upper cloud layers.

Finally we investigated the relationship between microphysical variables and cloud dilution for the resolved scale (150 m). The two-dimensional probability density function of AF and k shows that k decreases as AF decreases, from $k \sim 1$ for AF~ 1 to k between 0.75 and 0.85 for AF~ 0.1. To explain the linear relation between AF and k, we used a quantile regression of k with AF as the explanatory variable and found a positive slope. The probability density distribution of the CDNC versus the mean volume radius relative to their adiabatic values (i.e., the mixing diagram) showed that the model-simulated changes seem consistent with the theoretical prediction of inhomogeneous mixing. Such prediction is consistent with the turbulent mixing time scale estimated to be much larger than the microphysics time scale for the spatial scales resolved by the numerical model. Although with the analysis presented here there is still a scale gap between simulation and observation (~ 100 m versus ~ 10 m), a comparison of our results with the observational studies of (Burnet and Brenguier 2007; Brenguier et al. 2011) shows relatively good agreement for the microphysics and the way in which they are affected by entrainment. Consequently, we argue that the larger-scale microphysical variability is qualitatively well represented by the SDM.

By applying a prescribed kernel to spatially averaged model results, the present study focuses on the volume mean statistics and their comparison with observed values as opposed to exploring the sensitivity of microphysical variability to the spatial resolution. We leave for future study an investigation of microphysical sensitivity to spatial resolution with an increase in the effective spatial resolution to ~ 10 m, as in the in-situ aircraft observations.

Acknowledgments. The numerical model SCALE-RM (Scalable Computing for Advanced Library and Environment-Regional Model) was mainly developed at RIKEN Research Center for Computational Science (R-CCS). Part of the results in this study were obtained using the K computer (Project ID: ra001010) in RIKEN R-CCS and Oakbridge-CX in the Information Technology Center, the University of Tokyo. This work was supported by JSPS KAKENHI, Grant Numbers 19H01974 and 20K14559. The GFD-DENNOU Library (`www.gfd-dennou.org/library/dcl/`), Matplotlib (`matplotlib.org/`), and ParaView (`www.paraview.org/`) were used to draw the figures. WWG acknowledges partial support from the U.S. DOE ASR Grant DE-SC0016476. NCAR is sponsored by the National Science Foundation.

Data availability statement. The numerical model codes and configuration files used in this study are available at doi:10.5281/zenodo.4388632 (Matsushima et al. 2020).

References

Abade, G. C., W. W. Grabowski, and H. Pawlowska, 2018: Broadening of cloud droplet spectra through eddy hopping: Turbulent entraining parcel simulations. *J. Atmos. Sci.*, **75 (10)**, 3365–3379, https://doi.org/10.1175/JAS-D-18-0078.1.

Arabas, S., H. Pawlowska, and W. Grabowski, 2009: Effective radius and droplet spectral width from in-situ aircraft observations in trade-wind cumuli during rico. *Geophys. Res. Lett.*, **36 (11)**, https://doi.org/10.1029/2009GL038257.

Arabas, S., and S.-i. Shima, 2013: Large-eddy simulations of trade wind cumuli using particle-based microphysics with monte carlo coalescence. *J. Atmos. Sci.*, **70 (9)**, 2768–2777, https://doi.org/10.1175/JAS-D-12-0295.1.

Arabas, S., and S.-i. Shima, 2017: On the ccn (de)activation nonlinearities. *Nonlin. Processes Geophys.*, **24**, 535–542, https://doi.org/10.5194/npg-24-535-2017.

Baker, M., R. Corbin, and J. Latham, 1980: The influence of entrainment on the evolution of cloud droplet spectra: I. a model of inhomogeneous mixing. *Quart. J. Roy. Meteor. Soc.*, **106 (449)**, 581–598, https://doi.org/10.1002/qj.49710644914.

Bodenschatz, E., S. P. Malinowski, R. A. Shaw, and F. Stratmann, 2010: Can we understand clouds without turbulence? *Science*, **327 (5968)**, 970–971, https://doi.org/10.1126/science.1185138.

Brenguier, J.-L., T. Bourrianne, A. A. Coelho, J. Isbert, R. Peytavi, D. Trevarin, and P. Weschler, 1998: Improvements of droplet size distribution measurements with the fast-fssp (forward scattering spectrometer probe). *J. Atmos. Oceanic Technol.*, **15 (5)**, 1077–1090, https://doi.org/10.1175/1520-0426(1998)015<1077:IODSDM>2.0.CO;2.

Brenguier, J.-L., F. Burnet, and O. Geoffroy, 2011: Cloud optical thickness and liquid water path–does the k coefficient vary with droplet concentration? *Atmos. Chem. Phys.*, **11 (18)**, 9771–9786, https://doi.org/10.5194/acp-11-9771-201.

Brown, A. R., S. Derbyshire, and P. J. Mason, 1994: Large-eddy simulation of stable atmospheric boundary layers with a revised stochastic subgrid model. *Quart. J. Roy. Meteor. Soc.*, **120 (520)**, 1485–1512, https://doi.org/10.1002/qj.49712052004.

Burnet, F., and J.-L. Brenguier, 2007: Observational study of the entrainment-mixing process in warm convective clouds. *J. Atmos. Sci.*, **64 (6)**, 1995–2011, https://doi.org/10.1175/JAS3928.1.

Cooper, W. A., 1989: Effects of variable droplet growth histories on droplet size distributions. part I: Theory. *J. Atmos. Sci.*, **46 (10)**, 1301–1311, https://doi.org/10.1175/1520-0469(1989)046<1301:EOVDGH>2.0.CO;2.

Damiani, R., G. Vali, and S. Haimov, 2006: The structure of thermals in cumulus from airborne dual-doppler radar observations. *J. Atmos. Sci.*, **63 (5)**, 1432–1450, https://doi.org/10.1175/JAS3701.1.

Grabowski, W. W., 2020a: Comparison of eulerian bin and lagrangian particle-based schemes in simulations of pi chamber dynamics and microphysics. *Journal of the Atmospheric Sciences*, **77 (3)**, 1151–1165, https://doi.org/10.1175/JAS-D-19-0216.1.

Grabowski, W. W., 2020b: Comparison of eulerian bin and lagrangian particle-based microphysics in simulations of nonprecipitating cumulus. *Journal of the Atmospheric Sciences*, https://doi.org/10.1175/JAS-D-20-0100.1.

Grabowski, W. W., and G. C. Abade, 2017: Broadening of cloud droplet spectra through eddy hopping: Turbulent adiabatic parcel simulations. *J. Atmos. Sci.*, **74 (5)**, 1485–1493, https://doi.org/10.1175/JAS-D-17-0043.1.

Grabowski, W. W., and D. Jarecka, 2015: Modeling condensation in shallow nonprecipitating convection. *J. Atmos. Sci.*, **72 (12)**, 4661–4679, https://doi.org/10.1175/JAS-D-15-0091.1.

Grabowski, W. W., H. Morrison, S.-I. Shima, G. C. Abade, P. Dziekan, and H. Pawlowska, 2019: Modeling of cloud microphysics: Can we do better? *Bull. Amer. Meteor. Soc.*, **100 (4)**, 655–672, https://doi.org/10.1175/BAMS-D-18-0005.1.

Grabowski, W. W., and L.-P. Wang, 2013: Growth of cloud droplets in a turbulent environment. *Annu. Rev. Fluid Mech.*, **45**, 293–324, https://doi.org/10.1146/annurev-fluid-011212-140750.

Held, I. M., M. Zhao, and B. Wyman, 2007: Dynamic radiative–convective equilibria using gcm column physics. *Journal of the atmospheric sciences*, **64 (1)**, 228–238, https://doi.org/10.1175/JAS3825.11.

Heus, T., G. Van Dijk, H. J. Jonker, and H. E. Van den Akker, 2008: Mixing in shallow cumulus clouds studied by lagrangian particle tracking. *J. Atmos. Sci.*, **65 (8)**, 2581–2597, https://doi.org/10.1175/2008JAS2572.1.

Hudson, J. G., and S. S. Yum, 2001: Maritime–continental drizzle contrasts in small cumuli. *J. Atmos. Sci.*, **58 (8)**, 915–926, https://doi.org/10.1175/1520-0469(2001)058<0915:MCDCIS>2.0.CO;2.

Jarecka, D., W. W. Grabowski, H. Morrison, and H. Pawlowska, 2013: Homogeneity of the subgrid-scale turbulent mixing in large-eddy simulation of shallow convection. *Journal of the atmospheric sciences*, **70 (9)**, 2751–2767.

Knight, C. A., and L. J. Miller, 1998: Early radar echoes from small, warm cumulus: Bragg and hydrometeor scattering. *J. Atmos. Sci.*, **55 (18)**, 2974–2992, https://doi.org/10.1175/1520-0469(1998)055<2974:EREFSW>2.0.CO;2.

Koenker, R., and G. Bassett Jr, 1978: Regression quantiles. *Econometrica: journal of the Econometric Society*, 33–50, https://doi.org/10.2307/1913643.

Lasher-Trapp, S. G., W. A. Cooper, and A. M. Blyth, 2005: Broadening of droplet size distributions from entrainment and mixing in a cumulus cloud. *Quart. J. Roy. Meteor. Soc.*, **131 (605)**, 195–220, https://doi.org/10.1256/qj.03.199.

Lasher-Trapp, S. G., C. A. Knight, and J. M. Straka, 2001: Early radar echoes from ultragiant aerosol in a cumulus congestus: Modeling and observations. *J. Atmos. Sci.*, **58 (23)**, 3545–3562, https://doi.org/10.1175/1520-0469(2001)058<3545:EREFUA>2.0.CO;2.

Lehmann, K., H. Siebert, and R. A. Shaw, 2009: Homogeneous and inhomogeneous mixing in cumulus clouds: Dependence on local turbulence structure. *J. Atmos. Sci.*, **66 (12)**, 3641–3659, https://doi.org/10.1175/2009JAS3012.1.

Martin, G., D. Johnson, and A. Spice, 1994: The measurement and parameterization of effective radius of droplets in warm stratocumulus clouds. *J. Atmos. Sci.*, **51 (13)**, 1823–1842, https://doi.org/10.1175/1520-0469(1994)051<1823:TMAPOE>2.0.CO;2.

Matsushima, T., S.-i. Shima, and S. Nishizawa, 2020: SCALE-SDM source code and configuration files for Isolated cumulus congestus based on SCMS campaign. Zenodo, URL https://doi.org/10.5281/zenodo.4388632, https://doi.org/10.5281/zenodo.4388632.

Morrison, H., M. Witte, G. H. Bryan, J. Y. Harrington, and Z. J. Lebo, 2018: Broadening of modeled cloud droplet spectra using bin microphysics in an eulerian spatial domain. *J. Atmos. Sci.*, **75 (11)**, 4005–4030, https://doi.org/10.1175/JAS-D-18-0055.1.

Nishizawa, S., H. Yashiro, Y. Sato, Y. Miyamoto, and H. Tomita, 2015: Influence of grid aspect ratio on planetary boundary layer turbulence in large-eddy simulations. *Geosci. Model Dev.*, **8 (10)**, 3393–3419, https://doi.org/10.5194/gmd-8-3393-2015.

Sato, Y., S. Nishizawa, H. Yashiro, Y. Miyamoto, Y. Kajikawa, and H. Tomita, 2015: Impacts of cloud microphysics on trade wind cumulus: which cloud microphysics processes contribute to the diversity in a large eddy simulation? *Prog. Earth Planet Sci.*, **2 (1)**, 23, https://doi.org/10.1186/s40645-015-0053-6.

Sato, Y., S.-i. Shima, and H. Tomita, 2017: A grid refinement study of trade wind cumuli simulated by a lagrangian cloud microphysical model: the super-droplet method. *Atmos. Sci. Lett.*, **18 (9)**, 359–365, https://doi.org/10.1002/asl.764.

Sato, Y., S.-i. Shima, and H. Tomita, 2018: Numerical convergence of shallow convection cloud field simulations: Comparison between double-moment eulerian and particle-based lagrangian microphysics coupled to the same dynamical core. *J. Adv. Model. Earth Syst.*, **10 (7)**, 1495–1512, https://doi.org/10.1029/2018MS001285.

Shima, S.-i., K. Kusano, A. Kawano, T. Sugiyama, and S. Kawahara, 2009: The super-droplet method for the numerical simulation of clouds and precipitation: A particle-based and probabilistic microphysics model coupled with a non-hydrostatic model. *Quart. J. Roy. Meteor. Soc.*, **135 (642)**, 1307–1320, https://doi.org/10.1002/qj.441.

Siebert, H., H. Franke, K. Lehmann, R. Maser, E. W. Saw, D. Schell, R. A. Shaw, and M. Wendisch, 2006: Probing finescale dynamics and microphysics of clouds with helicopter-borne measurements. *Bulletin of the American Meteorological Society*, **87 (12)**, 1727–1738, https://doi.org/10.1175/BAMS-87-12-1727.

Siebert, H., and R. A. Shaw, 2017: Supersaturation fluctuations during the early stage of cumulus formation. *J. Atmos. Sci.*, **74 (4)**, 975–988, https://doi.org/10.1175/JAS-D-16-0115.1.

Skamarock, W. C., 2004: Evaluating mesoscale nwp models using kinetic energy spectra. *Mon. Wea. Rev.*, **132 (12)**, 3019–3032, https://doi.org/10.1175/MWR2830.1.

Stevens, B., and Coauthors, 2005: Evaluation of large-eddy simulations via observations of nocturnal marine stratocumulus. *Monthly weather review*, **133 (6)**, 1443–1462, https://doi.org/10.1175/MWR2930.1.

VanZanten, M. C., and Coauthors, 2011: Controls on precipitation and cloudiness in simulations of trade-wind cumulus as observed during rico. *J. Adv. Model. Earth Syst.*, **3 (2)**, https://doi.org/10.1029/2011MS000056.

Warner, J., 1955: The water content of cumuliform cloud. *Tellus*, **7 (4)**, 449–457, https://doi.org/10.3402/tellusa.v7i4.8917.

Yamaguchi, T., and D. A. Randall, 2012: Cooling of entrained parcels in a large-eddy simulation. *J. Atmos. Sci.*, **69 (3)**, 1118–1136, https://doi.org/10.1175/JAS-D-11-080.1.